Contents lists available at ScienceDirect

Bioactive Materials

Nucleotide coordinated polymers, a ROS-based immunomodulatory antimicrobial, doubly kill *Pseudomonas aeruginosa* biofilms of implant infections

Jinghuang Chen [a,b], Xianqing Tang [a,b], Qihan Sun [c], Xin Ji [a,b], Xingbo Wang [b,d], Zhendong Liu [b,d], Xu Zhang [d], Haijiao Xu [a], Fan Yang [a], Jian Sun [a,e,**], Xiurong Yang [a,b,*]

[a] *State Key Laboratory of Electroanalytical Chemistry, Changchun Institute of Applied Chemistry, Chinese Academy of Sciences, Changchun 130022, PR China*
[b] *School of Applied Chemistry and Engineering, University of Science and Technology of China, Hefei 230026, PR China*
[c] *Jilin Provincial Key Laboratory on Molecular and Chemical Genetic, The Second Hospital of Jilin University, Changchun 130022, PR China*
[d] *Changchun Institute of Applied Chemistry, Chinese Academy of Sciences, Changchun 130022, PR China*
[e] *College of Pharmacy, Xinjiang Medical University, Urumqi 830017, PR China*

ARTICLE INFO

ABSTRACT

Pseudomonas aeruginosa causes high morbidity and mortality in nosocomial infections, and newly approved antibiotics have been declining for decades. A green and universal deprotonation-driven strategy is used to screen the guanylic acid-metal ion coordination polymer nanoparticles (GMC), instead of the failure of binding occurs when specific metal ion participation. We find that the precise pH-dependent oxidase-like activity of GMC-2 orchestrates a duple symphony of immune modulation for *Pseudomonas aeruginosa* biofilm infections. Specifically, GMC-2-mediated reactive oxygen species (ROS) regulation triggers mitochondrial dysfunction and releases damage-associated molecular patterns, engaging pattern recognition receptors and resulting in endogenous innate immune activation. Meanwhile, GMC-2-triggered ROS generation in a mildly acidic biofilm environment destroys the biofilm, exposing exogenous pathogen-associated molecular patterns. GMC-2 cannot cause resistance for *Pseudomonas aeruginosa* compared with conventional antibiotics. In an infected implant mouse model, *Pseudomonas aeruginosa* biofilms were effectively eliminated by GMC-2-mediated triggering of innate and adaptive immunity. These findings provide a universal approach for facilitating the binding of biomolecules with metal ions and highlight the precise ROS-regulating platform plays a critical role in initiating endogenous and exogenous immune activation targeted for bacterial biofilm infection.

1. Introduction

Pseudomonas aeruginosa (*P. aeruginosa*), which causes high morbidity and mortality nosocomial infections in patients with orthopedic implants or cystic fibrosis, is one of the most virulent pathogenic organisms [1,2]. Clinically useful anti-*P. aeruginosa* antibiotics are limited, but their resistance is steadily increasing due to the low outer membrane permeability and effective efflux system, and newly approved antibiotics have been declining for decades [3]. Pathogens within biofilm shelters escape the host immune defense system by polarizing the host

immune cells to anti-inflammatory phenotypes and directly killing host immune cells [4–6]. In the post-antibiotic era, therapeutic approaches such as synergistic anti-biofilms and host immune activation have attracted considerable attention as a promising strategy to tackle recalcitrant *P. aeruginosa* biofilms [7,8].

Current bacterial immunotherapeutic strategies primarily focus on disrupting bacterial biofilms and releasing exogenous pathogen-associated molecular patterns (PAMPs), which engage pattern recognition receptors (PRRs) and activate host immune responses [5,9–12]. However, the host antibiofilm immune system is suppressed by

biofilm-generated exotoxins and quorum sensing systems, etc., resulting in a "cold" biofilm microenvironment [5,9]. Bacterial immune escape or even host immune paralysis is particularly severe due to the invasive secretion systems of gram-negative bacteria, particularly in *P. aeruginosa* with a type III secretion system (T3SS) [6,13–15]. Reprogramming the "cold" biofilm microenvironment to a "hot" one via spontaneous endogenous activation of the host immune system is a prerequisite for recognizing exogenous biofilm antigens and cascade catalysis of innate and adaptive immunity. Previous reports have suggested that reactive oxygen species (ROS) activate immune signaling and inflammatory signaling pathways, such as nuclear factor kappa-B (NF-κB), by disrupting dense biofilm structure and enabling pathogen destruction [10, 16–18]. However, endogenous activation of host immunity by ROS in bacterial immunotherapy is rarely reported, and its underlying mechanism has not been fully characterized.

Cellular stress and oxidative injury, partly derived from excess intracellular ROS, disrupt redox signaling and trigger mitochondrial DNA (mtDNA) release into the cytoplasm and extracellular space [16,19, 20]. mtDNA retains a resemblance to its bacterial origin (multiple copies, small size, and methylation status), engages PRRs, and is recognized by immune cells as "foreign" not "self" DNA [19,21–25]. It is called stress-induced damage-associated molecular patterns (DAMPs) [26], which endogenously activate the host immune response without the participation of exogenous biofilm antigens and are distinct from PAMPs. Therefore, we hypothesized that a well-designed ROS-regulating platform may initiate endogenous and exogenous immune responses to target bacterial biofilm infections by releasing exogenous biofilm antigens and endogenous mtDNA.

Coordination polymer nanoparticles (CPNs), self-assembled from nucleotides and metal ions (M^{n+}), have exhibited promise in versatile fields, including catalysis [27,28], bio-sensing [29,30], and nano-medicine [31,32]. Herein, a green and universal deprotonation-driven strategy was used to coordinate guanylic acid (GMP) with nutrient M^{n+} in an aqueous solution. This innovative strategy circumvents the failure of GMP-M^{n+} binding when specific metal ion participation [30–33]. Subsequently, we developed and screened GMP-Mn^{2+} CPNs-2 (GMC-2) with precise pH-dependent oxidase-like activity, orchestrating a duple symphony of immune modulation. Specifically, GMC-2-mediated ROS regulation triggered mitochondrial dysfunction and released DAMPs, engaging PRRs and resulting in endogenous innate immune activation. Meanwhile, GMC-2-triggered ROS generation in a mildly acidic biofilm environment destroyed the biofilm, exposing exogenous PAMPs. Moreover, GMC-2 cannot cause resistance for *P. aeruginosa* compared with conventional antibiotics. In an infected implant mouse model, *P. aeruginosa* biofilms were effectively eliminated by GMC-2-mediated triggering of innate and adaptive immunity. Taken together, this study provided a universal approach for facilitating the binding of biomolecules with M^{n+}, and highlighted that the precise ROS-regulating platform plays a critical role in initiating endogenous and exogenous immune responses targeted for biofilm infection (Scheme 1).
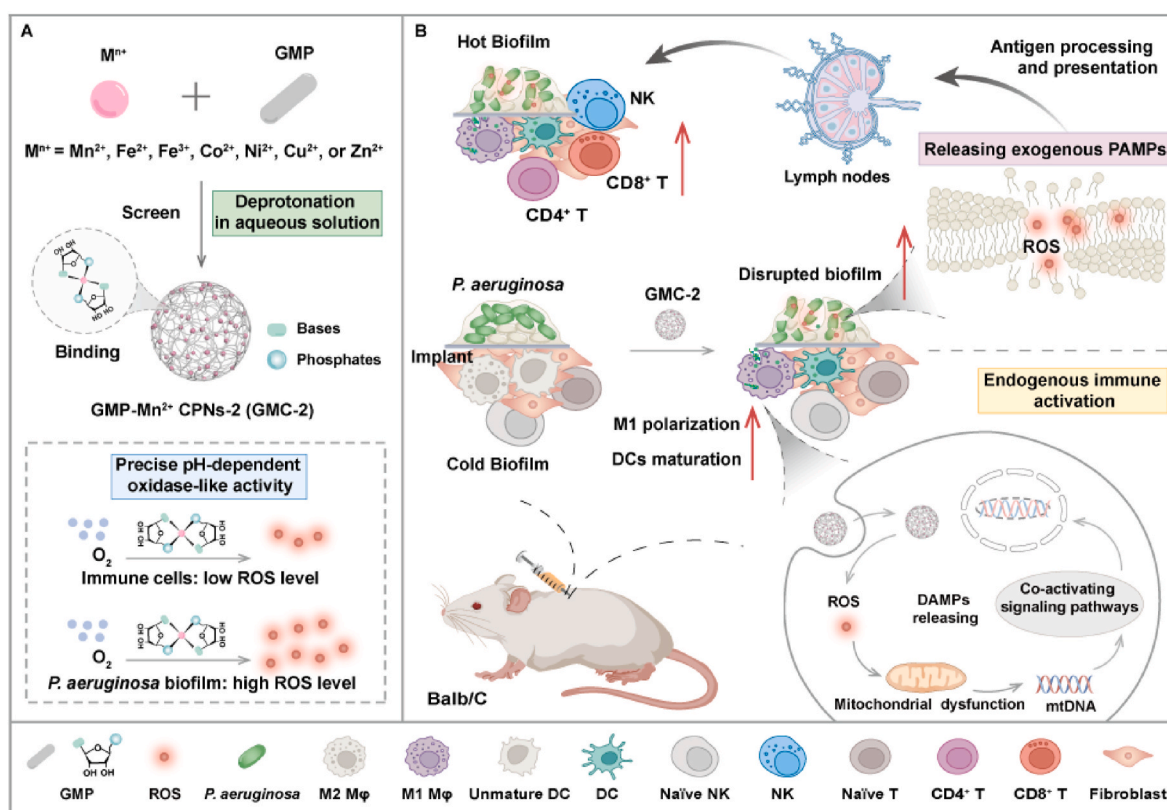
Scheme 1. Illustrating the preparation of immunomodulatory antimicrobial, and the mechanism of duple symphony for *Pseudomonas aeruginosa (P. aeruginosa)* biofilm infections. (A) An innovative and universal deprotonation-driven strategy for coordinating guanylic acid (GMP) with M^{n+}, circumvents the failure of GMP-M^{n+} binding when specific metal ion participation, and develops GMP-Mn^{2+} coordination polymer nanoparticles-2 (GMP-Mn^{2+} CPNs-2, termed GMC-2) with precise pH-dependent oxidase-like activity. (B) GMC-2-mediated reactive oxygen species (ROS) regulation triggers mitochondrial dysfunction and releases damage-associated molecular patterns (DAMPs), engaging pattern recognition receptors (PPRs) and resulting in endogenous innate immune activation. Meanwhile, GMC-2-triggered ROS generation in a mildly acidic biofilm environment destroys the biofilm, exposing exogenous pathogen-associated molecular patterns (PAMPs). *P. aeruginosa* biofilms can be effectively eliminated by the precise ROS-regulating platform triggering endogenous and exogenous immune responses.

2. Materials and methods

2.1. Density functional theory calculations

The reactive site of the GMP molecule was studied by using density functional theory (DFT) with the B3LYP method and def2-SVP basis set in the Gaussian 09 package. Harmonic vibrational frequency calculations were performed at the same theoretical level to guarantee that the molecule was at the minimum of the potential energy surface with no imaginary frequencies. The molecular electrostatic potential (ESP) was calculated using Multiwfn 3.8 (dev), with the input file extracted from formatted checkpoint files obtained from Gaussian and visualized using VMD 1.9.3. The Gibbs free energies of oxygen reduction reaction (ORR) intermediates in the reaction pathways were calculated from the computational hydrogen electrode model according to Nørskov et al. [34]. The reversible hydrogen electrode was regarded as a reference, then the chemical potential of the H^+/e^- pair was equal to half of the gas-phase H_2 at 0 V potential and 1 atm. The O reduction with a four-electron pathway in the free energy profile was calculated according to previous reports and all above calculations comprised water as an implicit solvent at the Solvation model density (SMD) [35].

2.2. Preparation of GMP-M^{n+} precipitates

Preparation of GMP-M^{n+} precipitates in NaOH aqueous solution. Volumes of 0, 20, 40, 60, 100, 200, and 400 μL NaOH aqueous solution (1 M) were added to the aqueous solution (5 mL, 10 mM) of GMP (Aladdin, China). The resulting mixtures were then combined with aqueous solutions of M^{n+} (5 mL, 10 mM). Suspensions were reacted for 2 h at room temperature with vigorous stirring. But for Co^{2+} (0 μL) and Co^{2+} (20 μL), the reaction times were extended to 3 and 24 h, respectively. The pH of the suspensions was measured by a pH meter (Sartorius, PB-10, Germany) after being reacted for 2 h, and the resulting precipitate was collected by three washes with 10 mL of deionized water. The preparation of GMP-M^{n+} precipitates in $NH_3 \cdot H_2O$ aqueous solution was similar to that in NaOH aqueous solution. Volumes (0, 20, 50, 100, and 200 μL) of $NH_3 \cdot H_2O$ aqueous solution (25 %) were added to the GMP aqueous solution. The product synthesis was optimized by changing the volume of $NH_3 \cdot H_2O$ added and the reaction time. Products formed from reactions with 0, 20, 50, 100, and 200 μL $NH_3 \cdot H_2O$ aqueous solution for 2 h were defined as GMC-0, GMC-1, GMC-2, GMC-3, and GMC-4, respectively. Preparation of GMP-M^{n+} precipitates in HEPES buffer and deionized water was based on previously reported methods [32,33,36–38].

2.3. Oxidase-like activity evaluation

Oxidase activities were evaluated with colorimetric assays [35]. GMP-M^{n+} CPNs (10 μL, 0.1 mg mL^{-1}) and TMB (Sigma-Aldrich, 10 μL, 10 mM) were added into 980 μL air-saturated sodium acetate–acetic acid buffer (pH 4.0, 20 mM). The catalytic oxidation of TMB was assessed by measuring the absorption of the oxidized form of TMB (oxTMB) at λ_{max} = 652 nm (ε = 39,000 M^{-1} cm^{-1}) using a UV–vis spectrophotometer (Varian, Cary 50, USA). To optimize the reacted conditions of GMC-2, a range of temperatures (10 °C–100 °C) and pH values (3.8–9.2) for the reaction were measured under the same conditions abovementioned. Reaction kinetics were measured under optimized conditions (pH 4.5, 20 mM air-saturated sodium acetate–acetic acid buffer).

2.4. Immune agonist screening and identification

RAW264.7 cells (TCM13, Cell Bank, Chinese Academy of Sciences) were co-cultured with 25 μg mL^{-1} GMP-M^{n+} CPNs in DMEM (10 % FBS) for 24 h, and then the level of IFN-β in supernatants was tested using a mouse IFN-β ELISA kit (Bio-Techne, USA) after centrifugation. The levels of proinflammatory factors (TNF-α, IL-1β, and IL-6) in supernatants were determined using mouse TNF-α, IL-1β, and IL-6 ELISA kits (Beyotime, China), respectively [39]. The intracellular ROS and DNA damage level of RAW264.7 cells were stained with a Reactive Oxygen Species Assay kit and DNA Damage Assay kit (Beyotime, China), and its fluorescence images were obtained with a fluorescence microscopy (Olympus, IX83, Japan). The cytosolic mtDNA level of RAW264.7 cells was tested using TaqMan™ Fast Advanced Master Mix (Thermo Fisher Scientific, USA) with a Real-Time PCR System (Bio-Rad, CFX Connect™, USA), and 18s RNA was used as an internal reference gene; primer sequences were listed in Table S4. Trizol (Beyotime, China) was added to extract the RNA of RAW264.7 cells and then immediately frozen in liquid nitrogen. Samples were sequenced by next-generation sequencing with the Illumina platform (Personalbio, China).

2.5. Anti-biofilm activity was assessed

A suspension of *P. aeruginosa* (1 × 10^6 CFU mL^{-1}) (ATCC 27853) was added to a 24-well plate containing sterile titanium plates (10-mm diameter). After incubation for 24 h, wells were washed three times with PBS to remove planktonic bacteria. The titanium plates with biofilm were then transferred into a new 24-well plate containing 1 mL LB medium and 1 mL working solution (sterile water, ampicillin, GMC-2). Then, the obtained bacterial suspensions were diluted with 2 mL PBS (10 mM, pH 5.5). The final working concentrations of ampicillin (Aladdin, China) and GMC-2 were both 100 μg mL^{-1}. After incubation for a further 24 h at 37 °C, the titanium plates were washed with PBS to remove planktonic bacteria. The biofilm was stained by LIVE/DEAD® BacLight™ Bacterial Viability Kits (Thermo Fisher Scientific, USA). The 3D images of *P. aeruginosa* biofilm were generated using a laser scanning confocal microscope (Zeiss, LSM 880, Germany). To quantify the biomass of biofilm, the biofilm was detached from the plates into 2 mL of PBS. Next, the suspensions (100 μL) were diluted into 2 mL of PBS and stained with a LIVE/DEAD® BacLight™ Bacterial Viability kit. The biofilm biomass was evaluated using a flow cytometer (Luminex, Guava® EasyCyte™, USA).

2.6. Treatment of medical-implant infection in animal models

Before treatment, mice were acclimatized for 1 week. A medical-implant infection animal model was constructed according to previously proposed methods [5,40]. Male BALB/c mice (six to eight weeks old, n = 30) were anesthetized via intraperitoneal injection of 1 % sodium pentobarbital (Sigma-Aldrich, USA), and their backs were shaved and disinfected [41]. Subsequently, sterile titanium plates (5-mm diameter) were inserted into subcutaneous layers in the backs of the mice, and the wounds were sutured. *P. aeruginosa* suspensions (100 μL, 1 × 10^6 CFU mL^{-1}) were injected into the implants subcutaneously. The following day, infected mice with implants were randomly divided into three groups, and 100 μL of sterile water (Control group), 2 mg kg^{-1} ampicillin (Ampicillin group), or 2 mg kg^{-1} GMC-2 (GMC-2 group) were subcutaneously administrated into the infected area of the implants. Considering the toxicity and antibacterial properties of antibiotics, we applied ampicillin with a lower dose. Based on the principle of administering 0.005 mL drug solution (400 μg mL^{-1} ampicillin or 400 μg mL^{-1} GMC-2) per g body weight of mice, the drug concentration is equivalent to 2 mg kg^{-1}. The infected skin of each mouse was then photographed on days 0, 1, 2, 3, 4, and 5. Mice were euthanized on day 5 after the operation, and the tissue samples (surrounding the infected skin) were excised. Then, tissue samples were fixed with 10 % paraformaldehyde and stained. All quantitative analyses were performed using ImageJ (v1.53e) or ImageJ Pro Plus (v6.0).

2.7. Statistical analysis

All results were presented as mean ± SD. Data were analyzed by GraphPad Prism (v 8.0.1), Origin 2023, or Excel 2019 unless otherwise

stated. Statistical analyses were performed using a one-way ANOVA (two-tailed). A p-value of <0.05 was indicated as statistically significant.

3. Results and discussion

3.1. Preparation and characterization of ROS-regulating platforms

To construct ROS-regulating platforms, theoretical calculations and experiments were used (Fig. 1A). The molecular electrostatic potential (ESP) of GMP (Fig. 1B), calculated using the density functional theory (DFT), demonstrated the favorable reactive site order is the position between N7 and O6 (−0.1302 Hartree), O in P=O, N9, N3, and Pα when the transition metal ion approaches the GMP molecule [42,43]. The H8 signal obviously broadened and shifted downfield relative to the ^{1}H nuclear magnetic resonance (NMR) of GMP (Fig. 1C), suggesting a possible binding site near N7 [28]. GMP ^{31}P and ^{13}C NMR (Fig. 1D and Fig. S1) further suggested near Pα as another potential binding site [27]. To predict molecular oxygen reduction by GMP-M^{n+} CPNs based on the
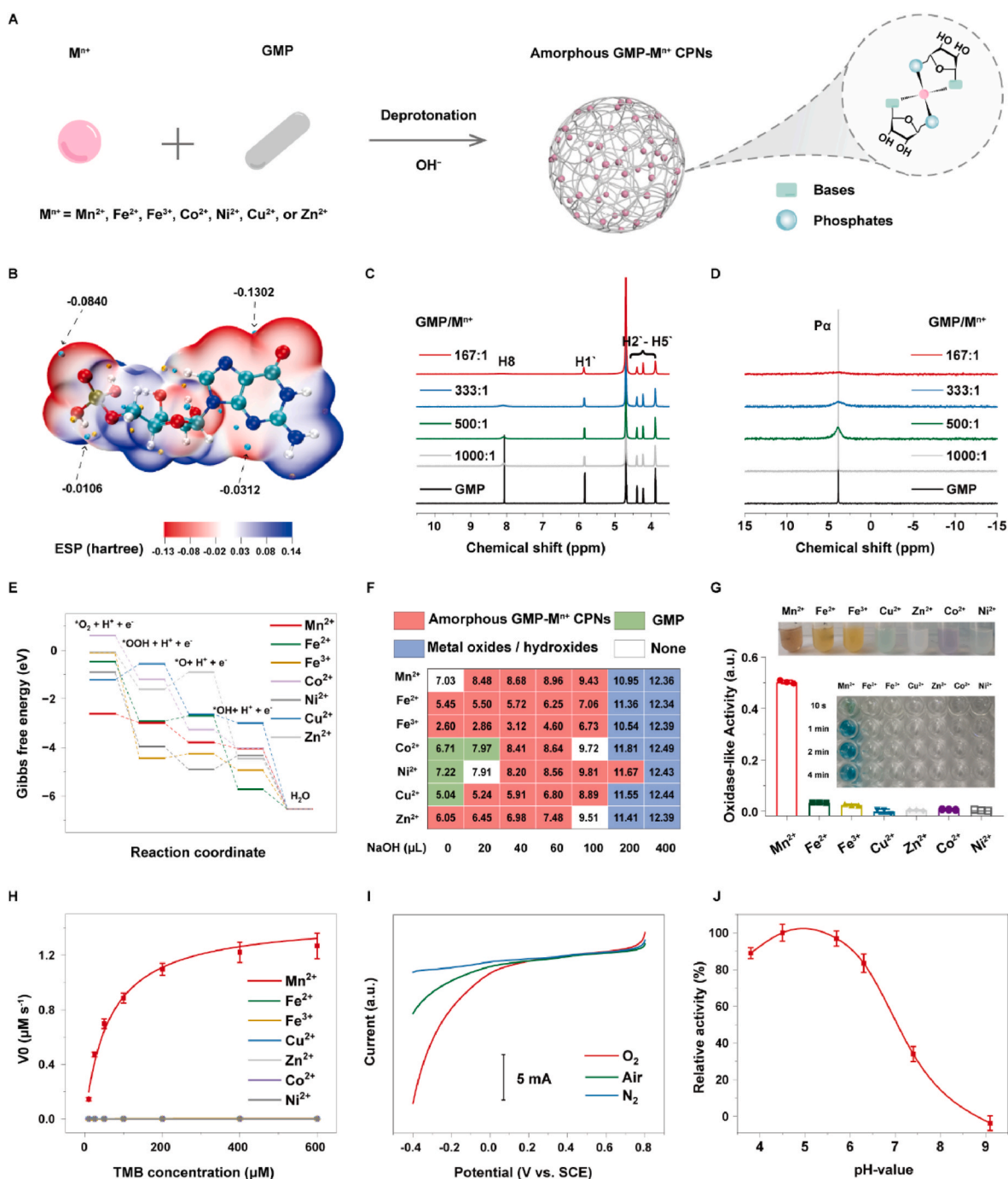

Fig. 1. Preparation and characterization of the ROS-regulating platforms. (A) Schematic depicting the GMP-M^{n+} CPNs synthetic route. (B) Electrostatic potential (ESP) plot of GMP. (C) ^{1}H and (D) ^{31}P NMR titrations of GMP with MnCl$_2$ in D$_2$O. (E) Gibbs free energy profile for oxygen reduction reaction on GMP-M^{n+} CPNs. (F) State summary for GMP-M^{n+} precipitates; pH value of each reaction is shown. (G) Oxidase-like activity of typical amorphous GMP-M^{n+} CPNs which of adding 60 μL 1 M NaOH solution (n = 3). The top inset is the amorphous GMP-M^{n+} CPNs in an aqueous solution. The middle inset is an optical image of the 3,3′,5,5′-tetramethylbenzidine (TMB) solution catalyzed by corresponding CPNs. (H) Michaelis–Menten curves of amorphous GMP-M^{n+} CPNs. (I) Polarization curves of GMC-2 detection currents under oxygen (O$_2$), air, or nitrogen (N$_2$). (J) Precise pH-dependent oxidase-like activity of GMC-2.

proposed four-electron pathway [35,44], we constructed an experimental structure model (Fig. S2). According to the Gibbs energetics (Fig. 1E and Table S1), GMP-Mn^{2+} CPNs exhibited the strongest oxidase-like activity.

Subsequently, we used four aqueous solution systems (NaOH, $NH_3 \cdot H_2O$, HEPES buffer, and deionized water) to test the reactivity between GMP and M^{n+} (Fig. S3–12). Progressive deprotonation in

NaOH and $NH_3 \cdot H_2O$ aqueous solutions yielded GMP crystallized precipitation, no precipitation, GMP-M^{n+} CPNs, and metal oxides/hydroxides (Fig. 1F). The GMP-M^{n+} CPNs structure was amorphous, as demonstrated by a pattern of X-ray diffraction (XRD) (Fig. S3–10), indicating M^{n+} binding with GMP. Amorphous CPNs were obtained by adding 60 μL of 1 M NaOH and a colorimetric 3,3′,5,5′-tetramethylbenzidine (TMB) assay was used to evaluate oxidase-like activity.
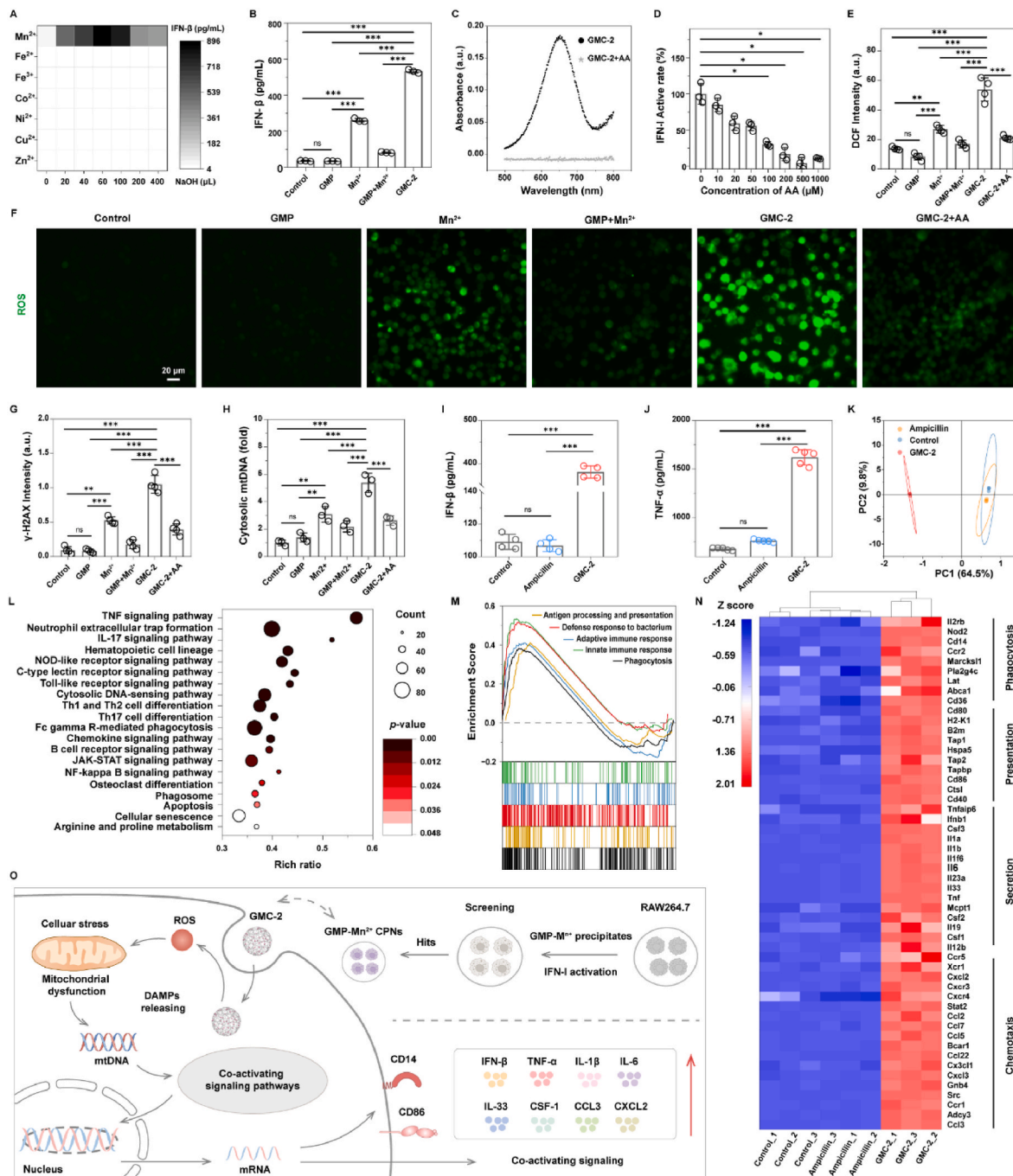

Fig. 2. Immune agonist screen and the mechanism of endogenous immune activation. (A) Interferon-β (IFN-β) concentration in the supernatants of RAW264.7 cells incubated with GMP-M^{n+} precipitates. (B) IFN-β concentration in the supernatants of different formulations (n = 3). (C) Reactive oxygen species (ROS) were scavenged by ascorbic acid (AA). (D) IFN-I activation of RAW264.7 cells at different AA concentrations (n = 3). (E) 2′,7′-dichlorofluorescein (DCF) fluorescence intensity (n = 4), (F) ROS fluorescence images, (G) γ-H2AX fluorescence intensity (n = 4), and (H) relative cytosolic mtDNA copy number with various treatments for RAW264.7 cells (n = 3). (I) IFN-β (n = 4) and (J) Tumor necrosis factor-α (TNF-α) (n = 5) concentration in the supernatants of RAW264.7 cells after different formulations. (K) Principal components analysis (PCA) plot, (L) Kyoto Encyclopedia of Genes and Genomes (KEGG) enrichment analysis, (M) Gene set enrichment analysis (GSEA), and (N) Heatmap showing differentially expressed genes from the transcriptome of RAW264.7 cells after different formulations; red, upregulation; blue, downregulation; $|\log_2$ fold change$| \geq 1$, $p < 0.05$. (O) Mechanism of endogenous immune activation by GMC-2. ns represents no significance, *$p < 0.05$, **$p < 0.01$, ***$p < 0.001$.

GMP-Mn^{2+} CPNs showed excellent oxidase-like activity, but the other constructs exhibited very little (Fig. 1G and Fig. S13), consistent with the theoretical prediction. Reaction kinetics (Fig. 1H and Table S2) further demonstrated that GMP-Mn^{2+} CPNs had excellent catalytic activity with O_2 (K_m = 63.565 μM, v_{max} = 1.463 μM s^{-1}) compared with the other GMP-M^{n+} CPNs, and previous reported enzyme-mimicking complexes [35,45–49]. We were surprised to note that "GMP-Mn^{2+} CPNs" prepared in HEPES buffer [30,33] had no oxidase-like activity (Fig. S11B), due to failure of GMP-Mn^{2+} binding, and were characterized as crystallized precipitation based on the characteristic diffraction peak of GMP (Fig. S11C). And similar events occurred in the Ni^{2+}, Co^{2+}-relevant reaction of the HEPES buffer reaction system and the Ni^{2+}, Co^{2+}, Cu^{2+}-relevant reaction of the deionized water reaction system. Therefore, we proposed the coordination of GMP with transition metals through a green and universal stepwise deprotonation-driven strategy.

Considering excellent oxidase-like activity, we optimized the reaction time (2 h) and the volume of $NH_3 \cdot H_2O$ (20 μL) for preparing GMP-Mn^{2+} CPNs (Figs. S14A–H). Optimized synthesis of GMC-2 yielded a hydrated particle size of 266.73 ± 2.27 nm with zeta potential −12.47 ± 0.32 mV (Figs. S15A and B), indicating GMC-2 is suitably stable in aqueous solution. The presence of Mn^{4+} (642.29 eV), Mn^{3+} (641.10 eV), and Mn^{2+} (640.10 eV) was confirmed by the X-ray photoelectron spectroscopy (XPS) analysis (Fig. S16), which suggested the catalytic performance of GMC-2 [50]. The most efficient oxygen reduction occurred in O_2, followed by air, and almost no activity occurred in nitrogen (Fig. 1I and Fig. S15E), confirming the innate oxidase-like activity of GMC-2 [35,51]. More importantly, the pH-responsive oxidase-like activity of GMC-2 subtly regulates ROS generation (approximately 97 % oxidase-like activity at pH 5.7, decreasing to 33 % at pH 7.4) (Fig. 1J), enabling bio-safe treatment approaches, in this case specific to biofilm infections [52]. Trapping agent experiments demonstrated that GMC-2 catalyzes O_2 to produce hydroxyl radical (•OH) and superoxide anions ($O_2^{\bullet-}$) (Fig. S15F), which prospectively regulate redox signaling and biological function via redox modifications of biological macromolecules [20].

3.2. Immune agonist screen and the mechanism of endogenous immune activation

To investigate type I interferon (IFN-I) activation, the levels of IFN-β were measured in the supernatant after incubating macrophages (RAW264.7, TCM13) with GMP-M^{n+} precipitates for 24 h (Fig. 2A). The IFN-β concentration associated with GMP-(Fe^{2+}, Fe^{3+}, Co^{2+}, Ni^{2+}, Cu^{2+}, or Zn^{2+}) precipitates did not differ significantly from that of the control group. By contrast, GMP-Mn^{2+} precipitates induced significantly higher IFN-β expression than the control group, which depended on the volume of NaOH added during the synthesis of these precipitates, and the strongest immune response arose when adding 60 μL of 1 M NaOH. It is necessary to note that after synthesizing these precipitates, we washed them three times with deionized water and excluded the residual NaOH's immune activation effect (Fig. S17A). Interestingly, the GMC-2 and Mn^{2+} groups showed 14.7-fold ($p < 0.001$) and 7.2-fold ($p < 0.001$) higher IFN-β concentration than the control group, respectively (Fig. 2B). However, the simple mixtures of GMP and Mn^{2+} did not trigger stronger immune activation than Mn^{2+} alone. These data demonstrate that the IFN-I activation in RAW264.7 cells was induced by the subtle synergy between GMP and Mn^{2+} in GMC-2. A moderate concentration of GMC-2 (25 μg mL^{-1}) was optimized for subsequent immune experiments (Fig. S17B). To reveal the mechanism of IFN-I activation, ascorbic acid (AA), a ROS scavenger, was loaded and the absorbance of oxTMB was reduced when AA was added into GMC-2 (Fig. 2C), demonstrating AA-mediated ROS removal. IFN-I activation was gradually suppressed with increasing AA concentration (Fig. 2D), demonstrating ROS-dependent IFN-I activation by GMC-2. A ROS burst was observed after GMC-2 excitation, but DCF fluorescence was

quenched by adding AA (Fig. 2E and F), providing additional evidence for the ROS-dependent IFN-I activation by GMC-2. Similar trends were observed in γ-H2AX immunofluorescence (Fig. 2G and Fig. S18) and cytosolic mtDNA (Fig. 2h), confirming that mitochondrial dysfunction was attributable to the excess intracellular ROS generated by GMC-2. Cytoplasmic mtDNA in the cytoplasm engages PRRs, rendering endogenous innate immune activation [16,19,21].

Ampicillin, a conventional beta-lactam antibiotic, was chosen as a clinical comparator due to its application in sterilization. Compared with the controls, the expression of IFN-β, tumor necrosis factor-α (TNF-α), interleukin-1β (IL-1β), and interleukin-6 (IL-6) was significantly higher in the presence of GMC-2 but similar in the presence of ampicillin (Fig. 2I, J and Fig. S19). We conclude that GMC-2 triggers immune activation, but ampicillin does not.

To profile the underlying mechanism of immune activation, bulk RNA sequencing (RNA-seq) was performed on RAW264.7 cells collected after 24 h of exposure to GMC-2 or ampicillin. Principal components analysis (PCA) and volcano map analysis (Fig. 2K and Fig. S20) revealed similar gene expression patterns in the ampicillin and control groups and significantly different patterns in the GMC-2 group. Kyoto Encyclopedia of Genes and Genomes (KEGG) enrichment analysis (Fig. 2L) demonstrated activation of immune and inflammatory pathways in the GMC-2 group, indicating that major coactivator signaling pathways were stimulated [5]. Other upregulated genes included antigen processing and presentation, defense response to the bacterium, innate immune response, adaptive immune response, and phagocytosis Gene Ontology gene sets in RAW264.7 treated with GMC-2 (Fig. 2M). Differentially expressed genes (DEGs) (|log2 fold change| ≥ 1, $p < 0.05$) are displayed in a heat map (Fig. 2N). Compared with the control and ampicillin groups, chemokine signaling genes *Ccl2*, *Ccl5*, *Ccl7*, *Cxcl3*, and *Cx3cl1* were upregulated by GMC-2. The C–C motif chemokine ligand 2 (CCL2) stimulates the secretion of antimicrobial peptides and recruits immune cells during microbial infections [53]. Cytokine related genes *Csf1*, *Csf2*, *Csf3*, *Ifnb1*, *Tnf*, *Il6*, and *Il1b* were significantly induced by GMC-2 relative to the control and ampicillin groups. Coactivator genes *Cd40*, *Cd80*, and *Cd86* were upregulated by GMC-2; these genes facilitate antigen processing and presentation, and license antigen-presenting cells to enhance T cell activation [5,10]. Phagocytosis-related genes *Cd14*, *Nod2*, and *Ccr2* were significantly induced by GMC-2. Cluster of differentiation 14 (CD14) recognizes and binds to bacterial lipopolysaccharides (LPS), and plays an important role in anti-infection immunity [54,55]. Furthermore, real-time fluorescence quantitative polymerase chain reaction (RT-qPCR) analysis verified the significantly increased expression of *Ifnb1*, *Cd86*, *Cd14*, *Csf1*, *Csf3*, *Ccl3*, *Cxcl2*, *Cxcl10*, and *Il33* in the presence of GMC-2 versus the control and ampicillin groups (Fig. S21). Accumulating evidence indicates that GMC-2 triggers endogenous immune activation by releasing mtDNA, stimulating coactivator signaling pathways, and upregulating IFN-I and proinflammatory factors (Fig. 2O).

3.3. Exogenous pathogen-associated antigen release

The release of pathogen-associated antigens initiates the adaptive immune response and alleviates immune escape, which marks a pivotal issue to profit biofilm-targeted immunotherapy [5,9,10]. We initially assessed GMC-2 against planktonic *P. aeruginosa* and found its minimum inhibitory concentration (MIC) was 100 μg mL^{-1} (Fig. 3A). SEM imaging confirmed the favorable antibacterial activity and structural deformation of the *P. aeruginosa* cell wall after GMC-2 exposure (Fig. 3B). Antibacterial activity was derived from the synergistic effects of GMP and Mn^{2+} in GMC-2 rather than from any single component (Fig. 3C and D). Compared with the control and ampicillin groups, ROS production was significantly higher in the GMC-2 group, as demonstrated by flow cytometry (Fig. 3E and Fig. S22A). Crystal violet staining [56,57] and quantitative analysis demonstrated the concentration-dependent antibacterial biofilm activity of GMC-2 (Fig. S23). Live/dead staining and
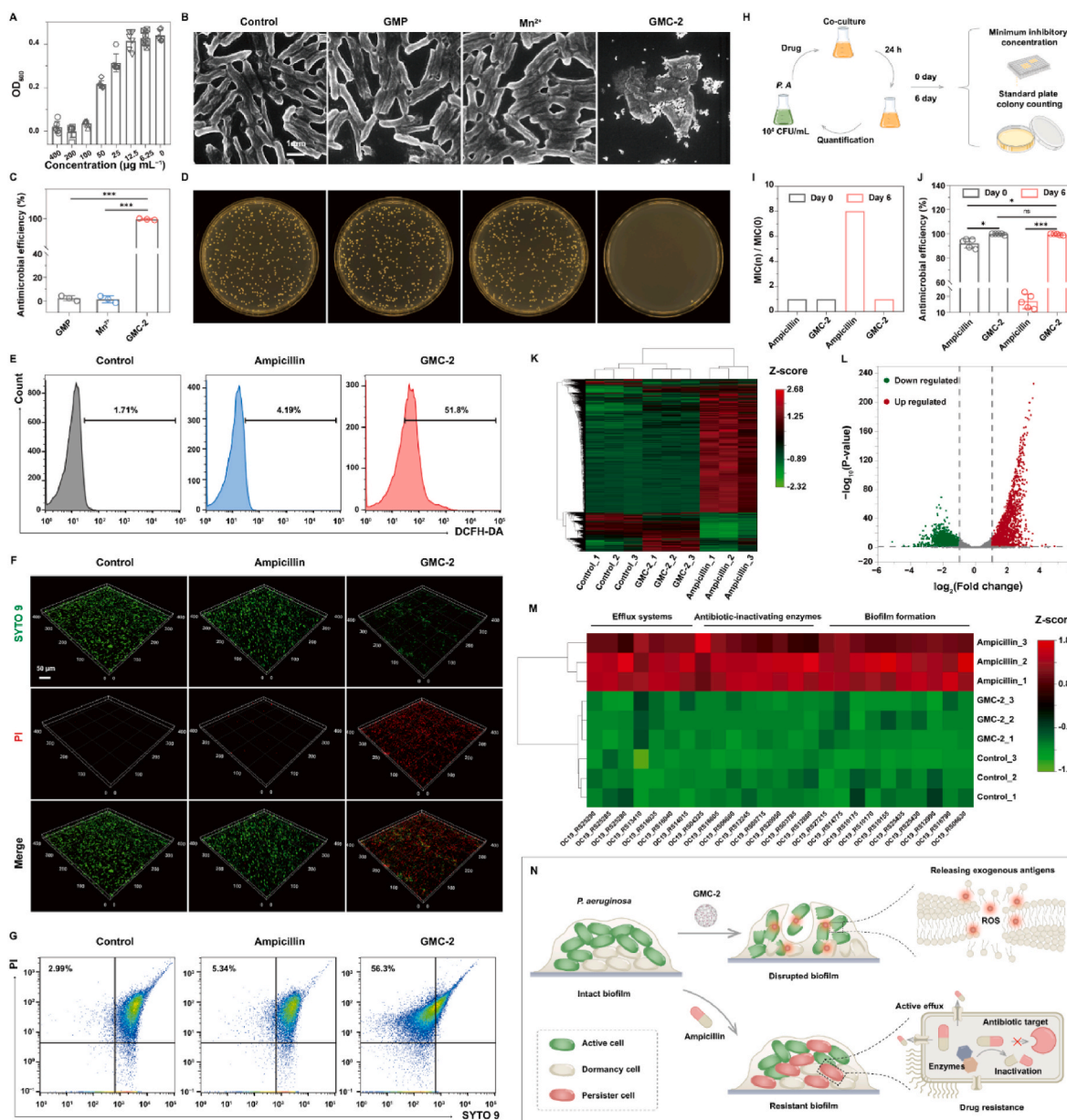
Fig. 3. Exogenous pathogen–associated antigen release. (A) Antibacterial activity of GMC-2 for planktonic *P. aeruginosa* (n = 4). (B) Representative scanning electron microscopy (SEM) images of *P. aeruginosa* after different formulations. (C) Antibacterial efficiency of GMP, Mn^{2+}, and GMC-2 for *P. aeruginosa* (n = 3). (D) Images of bacterial colony counts. (E) Typical flow cytometry plots of DCF fluorescence intensity in *P. aeruginosa*. (F) 3D confocal micrographs and (G) Representative flow cytometry plots of Syto 9/PI staining for *P. aeruginosa* biofilms. (H) Assessment of *P. aeruginosa* drug resistance. (I) Minimum inhibitory concentration (MIC) and (J) Antibacterial efficiency for *P. aeruginosa* (n = 5). (K) Whole genes, (L) Volcano plot and (M) Drug resistance genes from the transcriptome of *P. aeruginosa*; red, upregulation; green, downregulation; $|log_2$ fold change$| \geq 1$, $p < 0.05$. (N) Mechanism of exogenous pathogen-associated antigen release from *P. aeruginosa* biofilms by GMC-2. $*p < 0.05$, $**p < 0.01$, $***p < 0.001$.

3D confocal imaging (Fig. 3F) showed that GMC-2 destroyed *P. aeruginosa* biofilms, whereas the *P. aeruginosa* biofilms maintained their basal integrity in the control and ampicillin groups. Flow cytometry (Fig. 3G and Fig. S22B) demonstrated a significant reduction in biofilm biomass in response to GMC-2 but a negligible reduction in response to ampicillin versus the control group. Bacterial biofilm destruction and exposure of damaged bacteria are vital for exogenous bacterial antigen processing and presentation in the host [11].

Apart from biofilm formation, intrinsic resistance, and gene mutations contribute to drug resistance in *P. aeruginosa* [58]. To assess the drug resistance, 1×10^6 CFU mL^{-1} planktonic *P. aeruginosa* was cocultured with $0.5 \times$ MIC ampicillin or GMC-2 for 24 h through six cycles (Fig. 3H). Compared to day 0, the MIC of ampicillin showed an

eight-fold increase by day 6, but that of GMC-2 showed a negligible increase, indicating the absence of resistance acquisition in the presence of GMC-2, while ampicillin developed severe resistance (Fig. 3I and Fig. S24). The antibacterial efficiency of GMC-2 did not differ between days 0 and 6 ($p = 0.8747$), but the antibacterial efficiency of ampicillin dramatically decreased from 92.07 % to 16.85 % ($p < 0.001$) (Fig. 3J and Fig. S25). Gene expression patterns in *P. aeruginosa* were analyzed by bulk RNA-seq, which showed similarities between the control and GMC-2 groups versus differences in the ampicillin group (Fig. 3K). We observed 2902 DEGs between GMC-2 and ampicillin groups under a threshold of $|log2$ fold change$| \geq 1$ and $p < 0.05$ (Fig. 3L). Compared with the ampicillin group, drug-resistance genes (such as genes in efflux systems, antibiotic-inactivating enzymes, and biofilm formation) were

negligibly upregulated in the GMC-2 group (Fig. 3M and Table S3), indicating that *P. aeruginosa* drug resistance is retarded by GMC-2 [13, 59,60]. Collectively, GMC-2 eliminates *P. aeruginosa* by ROS, thereby releasing exogenous bacteria–associated antigens from *P. aeruginosa* biofilm, and the ROS antimicrobials have a lower probability of causing drug resistance in comparison with ampicillin (Fig. 3N) [61].

3.4. Enhancing the immune response to bacteria

Eukaryotic host cells are damaged by T3SS virulence effectors, such as ExoT, ExoS, and ExoY [1,13,58]. Consistently, macrophages (RAW264.7) were killed by *P. aeruginosa* observed under a microscope (Fig. S26). To determine whether bacterial damage to host cells was
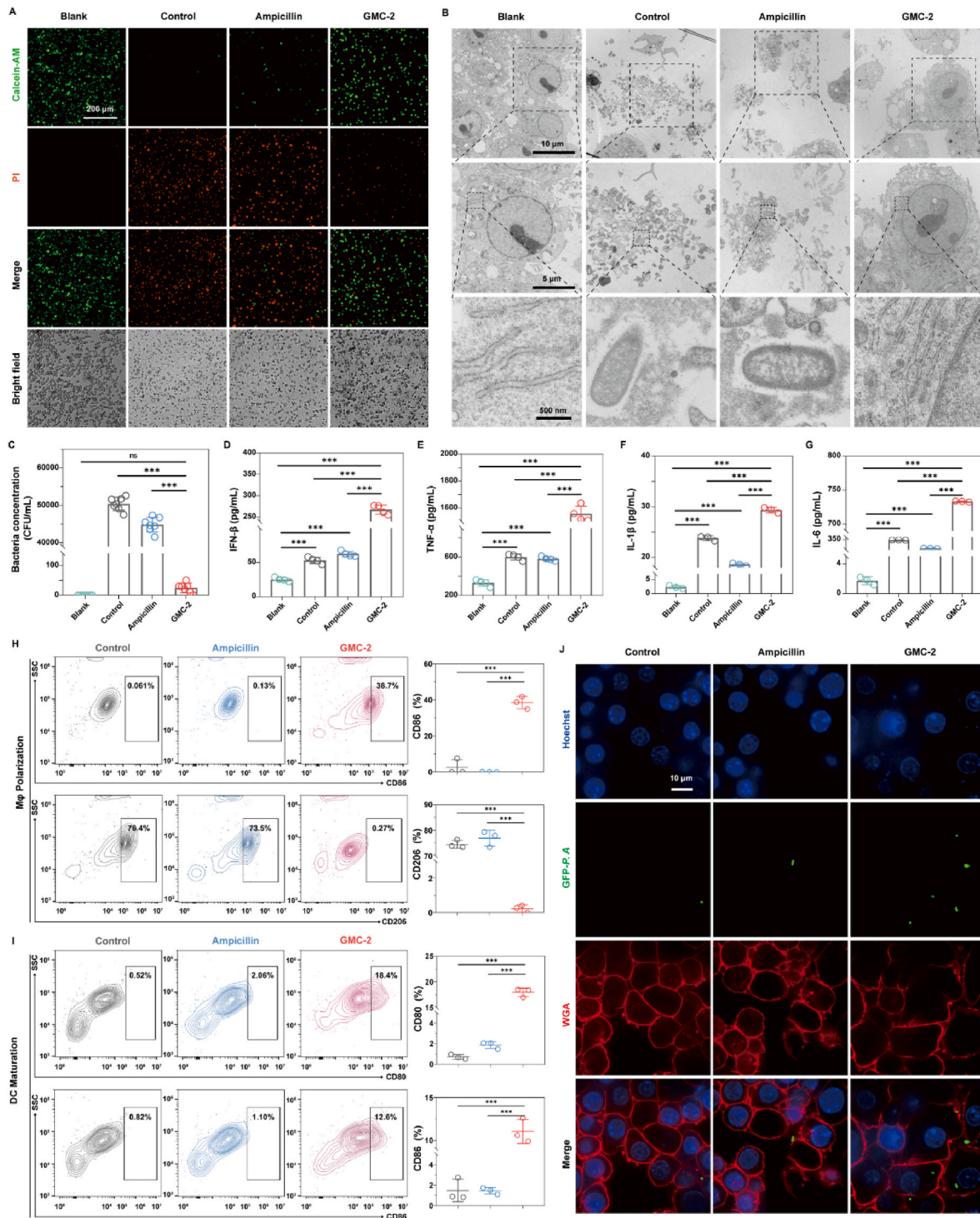

Fig. 4. Enhancing the immunity of immune cells to fight bacteria. (A) Live/dead staining microscope images and (B) Cryo-thin sectioning and transmission electron microscopy (TEM) images of RAW264.7 after incubation with *P. aeruginosa* and treatment for 24 h. (C) *P. aeruginosa* colony (n = 6), (D) IFN-β (n = 4), (E) TNF-α (n = 4), (F) IL-1β (n = 3), and (G) IL-6 (n = 3) concentration in supernatants of RAW264.7 incubated with *P. aeruginosa* after 24 h treatment. Representative flow cytometry plots and quantitative analysis (n = 3) of (H) mouse bone marrow-derived macrophages (BMDMs) and (I) mouse bone marrow-derived dendritic cells (BMDCs) after 24 h treatment. (J) Spinning–disk confocal laser scanning microscope images of RAW264.7 incubated with green fluorescent protein labeled *P. aeruginosa* (GFP-*P. A.*) after 1 h treatment and dyed by Hoechst and WGA. *$p < 0.05$, **$p < 0.01$, ***$p < 0.001$.

alleviated by GMC-2, RAW264.7 and *P. aeruginosa* co-suspensions were stained by Calcein-AM/PI kit after 24 h exposure to 0.25 × MIC GMC-2 and ampicillin. Controls included a bacteria-free blank and a bacterial control group. Compared with the control and ampicillin groups, the distinct stronger green fluorescence and apparent weaker red fluorescence were observed in the GMC-2 group, similar to the blank (Fig. 4A and Fig. S27), suggesting 0.25 × MIC GMC-2 duly alleviates *P. aeruginosa*–mediated damage to macrophage, while low concentration of ampicillin is incapable. Cryo-section and transmission electron

microscopy (TEM) imaging showed the destruction of RAW264.7 cells by invading bacteria in the control and ampicillin groups (Fig. 4B). In contrast, RAW264.7 remained healthy, with intact cell membranes, nuclei, and organelles in the GMC-2 and blank groups. In addition, bacterial counts (Fig. 4C and Fig. S28) showed significantly more bacterial colonies in the control and ampicillin groups compared with GMC-2 and blank groups ($p < 0.001$), which further confirms RAW264.7 cells have the upper hand in an environment with *P. aeruginosa* after GMC-2 exposure.
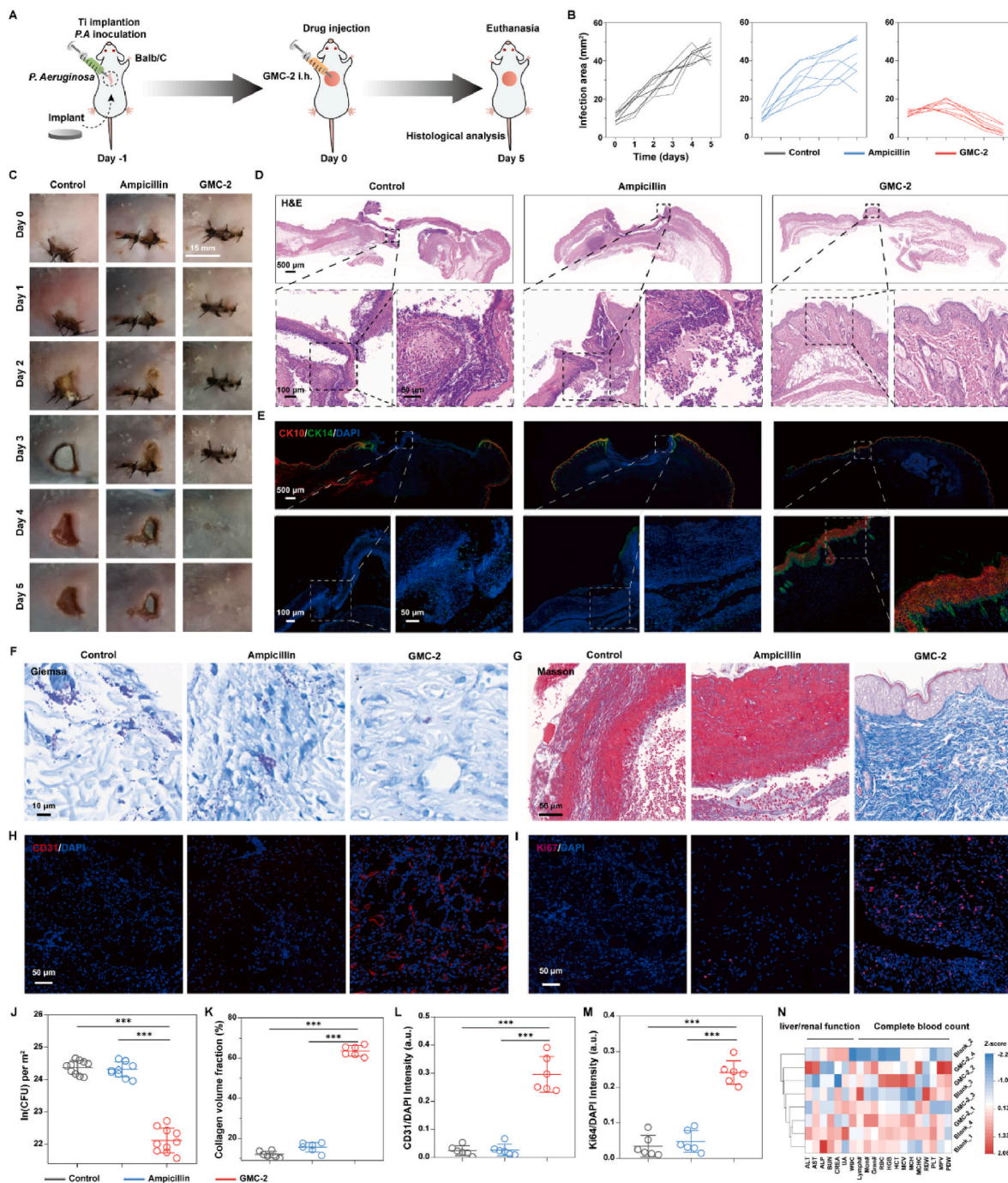

Fig. 5. Treatment of medical implant infection in a mouse model. (A) The scheme shows the construction of implant *P. aeruginosa* biofilm infection mouse model and drug administration. (B) Growth curves of individual infection area (n = 6). (C) Representative photo of operative regions after administrated. (D) Hematoxylin and eosin (H&E), (E) Cytokeratin10/cytokeratin14 (CK10/CK14) immunofluorescence, (F) Giemsa, (G) Masson, (H) CD31 immunofluorescence and (I) Ki67 immunofluorescence staining typical images of infected surrounding tissues after various treatments on day 5. (J)–(M) Quantitative analysis for individual histological staining, n = 10 for bacterial colony; n = 6 for collagen, CD31, and Ki67. (N) Heatmap showing liver/renal function and complete blood count to assess biocompatibility. *$p < 0.05$, **$p < 0.01$, ***$p < 0.001$.

To unfold the underlying mechanism of enhanced immune activity, we assayed several common IFN-I (IFN-β) and proinflammatory factors (TNF-α, IL-1β, and IL-6) in the supernatant of RAW264.7 cultured in suspension with *P. aeruginosa* (Fig. 4D–G). Notably, the control and ampicillin groups exhibited higher levels of IFN-I and pro-inflammatory factors than the bacteria-free blank, perhaps due to bacterial LPS secretion [55]. However, significantly higher levels of IFN-I and proinflammatory factors were detected in the GMC-2 group relative to the blank group ($p < 0.001$), control group ($p < 0.001$), and ampicillin group ($p < 0.001$). Given the inherent immune activation capacity of GMC-2, we proposed that GMC-2 enhances the immune capacity of macrophages (Mφ) against *P. aeruginosa* infection. Compared with the control and ampicillin groups, significant CD86 was upregulated and CD206 was downregulated of mouse bone marrow-derived macrophages (BMDMs) in the GMC-2 group (Fig. 4H), indicating GMC-2 spontaneously reprogrammed Mφ from an anti-inflammatory (M2) to pro-inflammatory (M1) phenotype [11]. Similarly, significant upregulated CD80 and CD86 of mouse bone marrow-derived dendritic cells (BMDCs) in the GMC-2 group were detected compared to control and ampicillin groups (Fig. 4I), indicating DCs was maturation induced by GMC-2, which may contribute to antigen presentation during bacterial infection [9,10]. To visualize the procession of Mφ engulfing bacteria, a green fluorescent protein labeled *P. aeruginosa* (GFP-*P. A.*) was constructed. The nucleus and cell membrane of RAW264.7 cells were stained with Hoechst and wheat germ agglutinin (WGA), respectively. After RAW264.7 cells were incubated with GFP-*P. A.* for 1 h, compared with control and ampicillin groups, the apparent GFP fluorescent signal of the GMC-2 group in RAW264.7 cells was observed by a spinning–disk confocal laser scanning microscope, and significantly more bacterial colonies in the GMC-2 group evaluated by the colony counting assay (Fig. 4J and Fig. S31). The results demonstrated that GMC-2 activated Mφ and promoted its engulfment of *P. aeruginosa*, and its defense bacterial infection as the first line of immune system defense.

3.5. Animal model of medical implant infection

Encouraged by the proper bactericidal and immune activation properties of GMC-2 *in vitro*, an implant *P. aeruginosa* biofilm infection mouse model was generated to assess the efficacy of GMC-2 *in vivo* (Fig. 5A) [5,40]. For comparison, drug-free and ampicillin-containing solutions were subcutaneously injected in BALB/c mice as negative controls. *P. aeruginosa* biofilm infection was basically limited and the sutured skin above the implants returned to its initial healthy state after 5 days in the GMC-2 group (Fig. 5B and C). Conversely, the skin gradually festered and the implants exposed or even shed in the control and ampicillin groups as infection progressed unabated. These data validated the efficacy of GMC-2 in treating medical implant *P. aeruginosa* biofilm infection.

To further evaluate treatment efficacy, the mice were euthanized on day 5 after administration, and the tissues surrounding the implant were excised for histological staining. Hematoxylin and eosin (H&E) staining (Fig. 5D) showed tissue destruction and infiltrating neutrophils in the control and ampicillin groups. In contrast, the skin tissues were structurally intact and showed little neutrophil infiltration in the GMC-2 group, indicating the implant-infected skin tissues had completed the inflammatory period and tissue repair [40]. Consistent with this, we identified a clearly stratified epithelium in the GMC-2 group versus damaged epithelial tissues in the control and ampicillin groups after immunofluorescent staining of cytokeratin10/cytokeratin14 (CK10/CK14) (Fig. 5E). Notably, typical Giemsa staining images (Fig. 5F) and quantitative analysis of bacterial biofilm biomass (Fig. 5J) demonstrated an efficient biofilm eradication by GMC-2 but bacteria remained in the skin tissues even on day 5 after administration in control and ampicillin groups. In addition, significant collagen deposition (Fig. 5G–K, and Fig. S32), vascular growth (Fig. 5H and L), and cell proliferation (Fig. 5I and M) were obtained in the GMC-2 group in

comparison with control and ampicillin groups. Altogether, GMC-2 overcomes inflammation by removing bacterial biofilms, enabling tissue repair.

To evaluate the biocompatibility of GMC-2, we first set up a blank control group without *P. aeruginosa* infection *in vivo* and performed assays on day 5. Insignificant differences were observed in complete blood count and renal and liver function between the blank control and GMC-2 groups (Fig. 5N, Figs. S33 and S34). H&E staining of the major organs (Fig. S35) revealed unobvious pathological effects of GMC-2 on the heart, liver, spleen, lung, kidney, and infected surrounding skin compared to the blank control group. However, H&E staining images demonstrated that ampicillin has mild liver and kidney toxicity in mice. Macroscopically, body weight curves (Fig. S36A) did not differ significantly between the GMC-2 and blank control groups. Additionally, the cytotoxicity and hemolysis rate testing (Figs. S36B and S36C) validated that GMC-2 is capable of biocompatibility.

3.6. Immunological analysis in vivo

Bacterial biofilm colonization creates a niche of immune depression in implant infections, and the T3SS of *P. aeruginosa* facilitates bacterial evasion of host immune responses to establish invasion, colonization, replication, and spread [6,13]. Given the bactericidal and immune activation properties of GMC-2, we preconceived that GMC-2 would eliminate *P. aeruginosa* biofilms via cooperative sterilization and reprogramming the biofilm microenvironment. To profile the immune mechanism of the antibiofilm effect, splenic immune cells were analyzed by flow cytometry 24 h after dosing (Fig. 6A). Notably, polarization of M1-phenotype macrophages (M1 Mφ, CD11b$^+$F4/80$^+$CD86$^+$CD206$^-$) in GMC-2 group was significantly higher than control group and ampicillin group (Fig. 6B). Consistent with this, we also observed more mature DCs (CD11c$^+$CD80$^+$CD86$^+$) in the GMC-2 group (Fig. 6C). Activated M1 Mφ and mature DCs reshape the "cold" biofilm microenvironment to a "hot" biofilm microenvironment [5,11,62]. They induce exogenous antigen (derived from biofilms) processing and presentation, triggering innate and adaptive immune cascades [10,17]. Moreover, the percentages of activated nature killer (NK) cells (CD49b$^+$CD107a$^+$) of the GMC-2 group were increased in comparison with control and ampicillin groups (Fig. 6D), demonstrating naïve NK cells were activated by GMC-2. The percentages of T helper cells (CD3$^+$CD4$^+$CD8$^-$) and cytotoxic T cells (CD3$^+$CD4$^-$CD8$^+$) were also increased by GMC-2 (Fig. 6E), indicating an activated adaptive response [10]. Similar trends of immune activation were confirmed in infection-draining lymph nodes (IDLN) (Fig. 6F–I). In addition, compared with the control and ampicillin groups, IFN-β, TNF-α, IL-1β, and IL-6 in serum were highly expressed in the GMC-2 group (Fig. 6J). Overall, GMC-2 activates Mφ, DCs, and NK cells, triggering the innate and adaptive immunity cascade against bacterial biofilm infections (Fig. 6K).

4. Conclusion

Collectively, we proposed a green and universal stepwise deprotonation-driven strategy to coordinate GMP with transition metals, instead of the failure of GMP-M^{n+} binding occurs in HEPES buffer and deionized water reaction system when specific metal ion participation [30,33]. Impressively, we screened amorphous GMP-Mn^{2+} CPNs with excellent oxidase-like activity ($K_m = 63.565$ μM, $\nu_{max} = 1.463$ μM s^{-1}) compared with other GMP-M^{n+} CPNs and reported enzyme-mimicking complexes. Subtly regulating ROS by GMC-2 renders mitochondrial dysfunction, and oxidative stress-inducing mtDNA (DAMPs) release into the cytoplasm, thereby engaging PRRs and resulting in endogenous innate immune activation of the host. Sufficient ROS generated by GMC-2 in a mildly acidic biofilm environment facilely destroyed bacterial biofilms, exposing exogenous bacteria–associated antigens (PAMPs). GMC-2 cannot cause resistance for *Pseudomonas aeruginosa* compared with ampicillin. GMC-2 (0.25 × MIC) duly
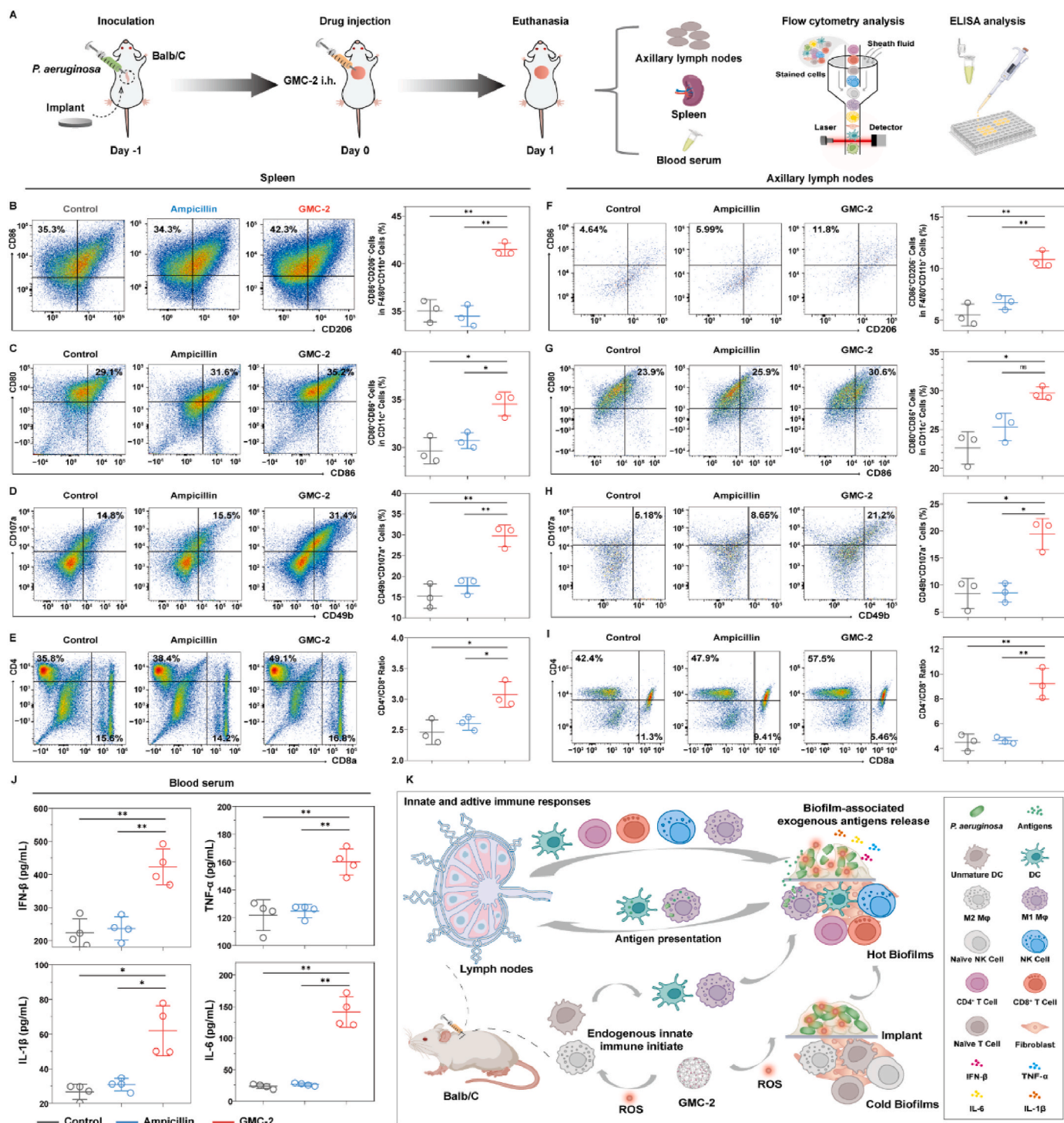
Fig. 6. Immunological analysis *in vivo*. (A) Scheme showing the processes of immunological analysis. Typical flow cytometry plots and quantitative analysis (n = 3) of (B) M1-phenotype macrophages (M1 Mφ, CD80$^+$CD206$^-$) by gating on CD11b$^+$F4/80$^+$ cells, (C) mature DCs (CD80$^+$CD86$^+$) by gating on CD11c$^+$ cells, (D) T helper cell (CD3$^+$CD4$^+$CD8$^-$), cytotoxic T cell (CD3$^+$CD4$^-$CD8$^+$), and (E) activated nature killer (NK) cells (CD107a$^+$) by gating on CD49b$^+$ cells in IDLN. (F)–(I) Corresponding plots and analyses in spleen. (J) IFN-β, TNF-α, IL-1β, and IL-6 concentrations of mouse in serum (n = 4). (K) Schematic depicting cascade catalyzing innate and adaptive immunity against bacterial biofilm infections by GMC-2. No significance is presented as ns, *$p < 0.05$, **$p < 0.01$, ***$p < 0.001$.

alleviates *P. aeruginosa* mediated macrophage damage, as opposed to a low concentration of ampicillin, which did not. Furthermore, *P. aeruginosa* biofilms were effectively eliminated by GMC-2 via triggering innate and adaptive immunity in a mouse model of implant infection, expediting the repair of infected tissue. This study provides a green and universal stepwise deprotonation-driven strategy, facilitating the binding of biomolecules with nutrient metal ions. Moreover, the

results of this study provide a paradigm for antibacterial immunotherapy with an unambiguous mechanism and highlight that the precise regulation of ROS is critical in initiating endogenous and exogenous immune responses to *P. aeruginosa* biofilm infections.

CRediT authorship contribution statement

Jinghuang Chen: Writing – review & editing, Writing – original draft, Methodology, Formal analysis, Data curation, Conceptualization. **Xianqing Tang:** Methodology, Investigation, Data curation. **Qihan Sun:** Methodology, Formal analysis, Data curation. **Xin Ji:** Software, Methodology, Investigation. **Xingbo Wang:** Software, Methodology. **Zhendong Liu:** Resources, Methodology. **Xu Zhang:** Validation, Resources. **Haijiao Xu:** Validation, Methodology. **Fan Yang:** Writing – review & editing, Supervision. **Jian Sun:** Writing – review & editing, Validation, Supervision, Project administration, Formal analysis. **Xiurong Yang:** Writing – review & editing, Supervision, Project administration, Funding acquisition.

Data availability

The data that support the findings of this study are available from the corresponding author upon reasonable request.

Ethics approval and consent to participate

All animal protocols were conducted following the guidelines of the Animal Care and Ethics Committee of Changchun Institute of Applied Chemistry, Chinese Academy of Sciences, and approved by the Institutional Animal Care and Use Committee (IACUC) for Animal Experiment (no. 20230175). All participants consented to publish the paper.

Declaration of competing interest

The authors declare that they have no conflict of interest.

Acknowledgments

Appendix A. Supplementary data

Supplementary data to this article can be found online at https://doi.org/10.1016/j.bioactmat.2024.10.026.

References

[1] M.W. Azam, A.U. Khan, Updates on the pathogenicity status of *Pseudomonas aeruginosa*, Drug Discov. Today 24 (1) (2019) 350–359, https://doi.org/10.1016/j.drudis.2018.07.003.

[2] J. Hu, Y. Ding, B. Tao, Z. Yuan, Y. Yang, K. Xu, X. Li, P. Liu, K. Cai, Surface modification of titanium substrate via combining photothermal therapy and quorum-sensing-inhibition strategy for improving osseointegration and treating biofilm-associated bacterial infection, Bioact. Mater. 18 (2022) 228–241, https://doi.org/10.1016/j.bioactmat.2022.03.011.

[3] B.K. Gorityala, G. Guchhait, D.M. Fernando, S. Deo, S.A. McKenna, G.G. Zhanel, A. Kumar, F. Schweizer, Adjuvants based on hybrid antibiotics overcome resistance in *Pseudomonas aeruginosa* and enhance fluoroquinolone efficacy, Angew. Chem. Int. Ed. 55 (2) (2016) 555–559, https://doi.org/10.1002/anie.201508330.

[4] B.B. Finlay, G. McFadden, Anti-immunology: evasion of the host immune system by bacterial and viral pathogens, Cell 124 (4) (2006) 767–782, https://doi.org/10.1016/j.cell.2006.01.034.

[5] C. Yang, Y. Luo, H. Shen, M. Ge, J. Tang, Q. Wang, H. Lin, J. Shi, X. Zhang, Inorganic nanosheets facilitate humoral immunity against medical implant infections by modulating immune co-stimulatory pathways, Nat. Commun. 13 (1) (2022) 4866, https://doi.org/10.1038/s41467-022-32405-x.

[6] C.R. Arciola, D. Campoccia, L. Montanaro, Implant infections: adhesion, biofilm formation and immune evasion, Nat. Rev. Microbiol. 16 (7) (2018) 397–409, https://doi.org/10.1038/s41579-018-0019-y.

[7] H. Etayash, Y. Qian, D. Pletzer, Q. Zhang, J. Xie, R. Cui, C. Dai, P. Ma, F. Qi, R. Liu, R.E.W. Hancock, Host defense peptide-mimicking amphiphilic beta-peptide polymer (Bu:DM) exhibiting anti-biofilm, immunomodulatory, and *in vivo* anti-infective activity, J. Med. Chem. 63 (21) (2020) 12921–12928, https://doi.org/10.1021/acs.jmedchem.0c01321.

[8] S. Zhang, H. Yang, M. Wang, D. Mantovani, K. Yang, F. Witte, L. Tan, B. Yue, X. Qu, Immunomodulatory biomaterials against bacterial infections: progress, challenges, and future perspectives, Innovation 4 (6) (2023) 100503, https://doi.org/10.1016/j.xinn.2023.100503.

[9] W. Zhu, J. Mei, X. Zhang, J. Zhou, D. Xu, Z. Su, S. Fang, J. Wang, X. Zhang, C. Zhu, Photothermal nanozyme-based microneedle patch against refractory bacterial biofilm infection via iron-actuated Janus ion therapy, Adv. Mater. 34 (51) (2022) 2207961, https://doi.org/10.1002/adma.202207961.

[10] L. Chen, Z. Shao, Z. Zhang, W. Teng, H. Mou, X. Jin, S. Wei, Z. Wang, Y. Eloy, W. Zhang, H. Zhou, M. Yao, S. Zhao, X. Chai, F. Wang, K. Xu, J. Xu, Z. Ye, An on-demand collaborative innate-adaptive immune response to infection treatment, Adv. Mater. (2023) 2304774, https://doi.org/10.1002/adma.202304774.

[11] W. Feng, G. Li, X. Kang, R. Wang, F. Liu, D. Zhao, H. Li, F. Bu, Y. Yu, T.F. Moriarty, Q. Ren, X. Wang, Cascade-targeting poly(amino acid) nanoparticles eliminate intracellular bacteria via on-site antibiotic delivery, Adv. Mater. 34 (12) (2022) 2109789, https://doi.org/10.1002/adma.202109789.

[12] R.S. Li, J. Liu, J. Wen, Y. Shi, J. Ling, Q. Cao, L. Wang, H. Shi, C.Z. Huang, N. Li, Transformable nano-antibiotics for mechanotherapy and immune activation against drug-resistant Gram-negative bacteria, Sci. Adv. 9 (34) (2023) eadg9601, https://doi.org/10.1126/sciadv.adg9601.

[13] S. Qin, W. Xiao, C. Zhou, Q. Pu, X. Deng, L. Lan, H. Liang, X. Song, M. Wu, *Pseudomonas aeruginosa*: pathogenesis, virulence factors, antibiotic resistance, interaction with host, technology advances and emerging therapeutics, Signal Transduct. Targeted Ther. 7 (1) (2022) 199, https://doi.org/10.1038/s41392-022-01056-1.

[14] J. Sponsel, Y. Guo, L. Hamzam, A.C. Lavanant, A. Perez-Riveron, E. Partiot, Q. Muller, J. Rottura, D. Hauck, A. Titz, V. Flacher, W. Romer, C. G. Mueller, *Pseudomonas aeruginosa* LecB suppresses immune responses by inhibiting transendothelial migration, EMBO Rep. 24 (4) (2023) e55971, https://doi.org/10.15252/embr.202255971.

[15] M.W. Hornef, M.J. Wick, M. Rhen, S. Normark, Bacterial strategies for overcoming host innate and adaptive immune responses, Nat. Immunol. 3 (2002) 1033–1040, https://doi.org/10.1038/ni1102-1033.

[16] K. Wang, Y. Li, X. Wang, Z. Zhang, L. Cao, X. Fan, B. Wan, F. Liu, X. Zhang, Z. He, Y. Zhou, D. Wang, J. Sun, X. Chen, Gas therapy potentiates aggregation-induced emission luminogen-based photoimmunotherapy of poorly immunogenic tumors through cGAS-STING pathway activation, Nat. Commun. 14 (1) (2023) 2950, https://doi.org/10.1038/s41467-023-38601-7.

[17] G. Guo, H. Zhang, H. Shen, C. Zhu, R. He, J. Tang, Y. Wang, X. Jiang, J. Wang, W. Bu, X. Zhang, Space-selective chemodynamic therapy of $CuFe_5O_8$ nanocubes for implant-related infections, ACS Nano 14 (10) (2020) 13391–13405, https://doi.org/10.1021/acsnano.0c05255.

[18] Y. Ma, H. Xu, B. Sun, S. Du, S. Cui, L. Zhang, N. Ding, D. Yang, pH-responsive oxygen and hydrogen peroxide self-supplying nanosystem for photodynamic and chemodynamic therapy of wound infection, ACS Appl. Mater. Interfaces 13 (50) (2021) 59720–59730, https://doi.org/10.1021/acsami.1c19681.

[19] Y. Lei, J.J. VanPortfliet, Y.-F. Chen, J.D. Bryant, Y. Li, D. Fails, S. Torres-Odio, K. B. Ragan, J. Deng, A. Mohan, B. Wang, O.N. Brahms, S.D. Yates, M. Spencer, C. W. Tong, M.W. Bosenberg, L.C. West, G.S. Shadel, T.E. Shutt, J.W. Upton, P. Li, A. P. West, Cooperative sensing of mitochondrial DNA by ZBP1 and cGAS promotes cardiotoxicity, Cell 186 (14) (2023) 3013–3032, https://doi.org/10.1016/j.cell.2023.05.039.

[20] H. Sies, V.V. Belousov, N.S. Chandel, M.J. Davies, D.P. Jones, G.E. Mann, M. P. Murphy, M. Yamamoto, C. Winterbourn, Defining roles of specific reactive oxygen species (ROS) in cell biology and physiology, Nat. Rev. Mol. Cell Biol. 23 (7) (2022) 499–515, https://doi.org/10.1038/s41580-022-00456-z.

[21] A.P. West, G.S. Shadel, Mitochondrial DNA in innate immune responses and inflammatory pathology, Nat. Rev. Immunol. 17 (6) (2017) 363–375, https://doi.org/10.1038/nri.2017.21.

[22] T. Zhang, C. Yin, A. Fedorov, L. Qiao, H. Bao, N. Beknazarov, S. Wang, A. Gautam, R.M. Williams, J.C. Crawford, S. Peri, V. Studitsky, A.A. Beg, P.G. Thomas, C. Walkley, Y. Xu, M. Poptsova, A. Herbert, S. Balachandran, ADAR1 masks the cancer immunotherapeutic promise of ZBP1-driven necroptosis, Nature 606 (2022) 594–602, https://doi.org/10.1038/s41586-022-04753-7.

[23] T.-t. Shi, Y. Huang, Y.L. Li, X.-l. Dai, Y.-h. He, J.-c. Ding, T. Ran, Y. Shi, Q. Yuan, W.-j. Li, W. Liu, MAVI1, an endoplasmic reticulum–localized microprotein, suppresses antiviral innate immune response by targeting MAVS on mitochondrion, Sci. Adv. 9 (35) (2023) eadg7053, https://doi.org/10.1126/sciadv.adg7053.

[24] G. Liu, Y. Zhang, H. Yao, Z. Deng, S. Chen, Y. Wang, W. Peng, G. Sun, M.-K. Tse, X. Chen, J. Yue, Y.-K. Peng, L. Wang, G. Zhu, An ultrasound-activatable platinum prodrug for sono-sensitized chemotherapy, Sci. Adv. 9 (25) (2023) eadg5964, https://doi.org/10.1126/sciadv.adg596.

[25] J. Saada, R.J. McAuley, M. Marcatti, T.Z. Tang, M. Motamedi, B. Szczesny, Oxidative stress induces Z-DNA-binding protein 1–dependent activation of microglia via mtDNA released from retinal pigment epithelial cells, J. Biol. Chem. 298 (1) (2022) 101523, https://doi.org/10.1016/j.jbc.2021.101523.

[26] A.N. Cheng, L.C. Cheng, C.L. Kuo, Y.K. Lo, H.Y. Chou, C.H. Chen, Y.H. Wang, T. H. Chuang, S.J. Cheng, A.Y. Lee, Mitochondrial Lon-induced mtDNA leakage contributes to PD-L1–mediated immunoescape via STING-IFN signaling and extracellular vesicles, J. Immunother. Cancer 8 (2) (2020) e001372, https://doi.org/10.1136/jitc-2020-001372.

[27] C. Wang, Q. Qi, W. Li, J. Dang, M. Hao, S. Lv, X. Dong, Y. Gu, P. Wu, W. Zhang, Y. Chen, J.S. Hartig, A Cu(II)-ATP complex efficiently catalyses enantioselective Diels-Alder reactions, Nat. Commun. 11 (1) (2020) 4792, https://doi.org/10.1038/s41467-020-18554-x.

[28] C. Wang, M. Hao, Q. Qi, J. Dang, X. Dong, S. Lv, L. Xiong, H. Gao, G. Jia, Y. Chen, J. S. Hartig, C. Li, Highly efficient cyclic dinucleotide based artificial metalloribozymes for enantioselective friedel-crafts reactions in water, Angew. Chem. Int. Ed. 59 (9) (2020) 3444–3449, https://doi.org/10.1002/anie.201912962.

[29] Y. Wang, Y. Liu, D. Tu, M. Chen, Y. Zhang, H. Gao, X. Chen, Tumor-microenvironment-responsive biodegradable nanoagents based on lanthanide nucleotide self-assemblies toward precise cancer therapy, Angew. Chem. Int. Ed. 61 (14) (2022) e202116983, https://doi.org/10.1002/anie.202116983.

[30] Y. Zhang, S. Liu, Q. Yuan, H. Liang, Zr-based acid-stable nucleotide coordination polymers: an excellent platform for acidophilic enzymes immobilization, J. Inorg. Biochem. 216 (2021) 111338, https://doi.org/10.1016/j.jinorgbio.2020.111338.

[31] Z. Luo, X. Liang, T. He, X. Qin, X. Li, Y. Li, L. Li, X.J. Loh, C. Gong, X. Liu, Lanthanide-nucleotide coordination nanoparticles for STING activation, J. Am. Chem. Soc. 144 (36) (2022) 16366–16377, https://doi.org/10.1021/jacs.2c03266.

[32] J. Zhao, X. Bao, T. Meng, S. Wang, S. Lu, G. Liu, J. Wang, J. Sun, X. Yang, Fe(II)-driven self-assembly of enzyme-like coordination polymer nanoparticles for cascade catalysis and wound disinfection applications, Chem. Eng. J. 420 (15) (2021) 129674, https://doi.org/10.1016/j.cej.2021.129674.

[33] H. Liang, F. Lin, Z. Zhang, B. Liu, S. Jiang, Q. Yuan, J. Liu, Multicopper laccase mimicking nanozymes with nucleotides as ligands, ACS Appl. Mater. Interfaces 9 (2) (2017) 1352–1360, https://doi.org/10.1021/acsami.6b15124.

[34] J.K. Nørskov, T. Bligaard, A. Logadottir, J.R. Kitchin, J.G. Chen, S. Pandelov, U. Stimming, Trends in the exchange current for hydrogen evolution, J. Electrochem. Soc. 152 (3) (2005) J23–J26, https://doi.org/10.1149/1.1856988.

[35] L. Huang, J. Chen, L. Gan, J. Wang, S. Dong, Single-atom nanozymes, Sci. Adv. 5 (5) (2019) eaav5490, https://doi.org/10.1126/sciadv.aav5490.

[36] H. Liang, B. Liu, Q. Yuan, J. Liu, Magnetic iron oxide nanoparticle seeded growth of nucleotide coordinated polymers, ACS Appl. Mater. Interfaces 8 (24) (2016) 15615–15622, https://doi.org/10.1021/acsami.6b04038.

[37] Y. Yang, J. Xu, Y. Guo, X. Wang, L.-P. Xiao, J. Zhou, Biodegradation of lignin into low-molecular-weight oligomers by multicopper laccase-mimicking nanozymes of the Cu/GMP complex at room temperature, ACS Sustainable Chem. Eng. 10 (17) (2022) 5489–5499, https://doi.org/10.1021/acssuschemeng.1c08679.

[38] Y. Wang, Y. Ding, D. Yao, H. Dong, C. Ji, J. Wu, Y. Hu, A. Yuan, Copper-based nanoscale coordination polymers augmented tumor radioimmunotherapy for immunogenic cell death induction and T-Cell infiltration, Small 17 (8) (2021) 2006231, https://doi.org/10.1002/smll.202006231.

[39] X. Cheng, H. Chen, F. Yang, J. Hong, Y. Cheng, J. Hu, All-small-molecule supramolecular hydrogels assembled from guanosine 5′-monophosphate disodium salt and tobramycin for the treatment of bacterial keratitis, Bioact. Mater. 16 (2022) 293–300, https://doi.org/10.1016/j.bioactmat.2021.12.024.

[40] X. Qu, M. Wang, M. Wang, H. Tang, S. Zhang, H. Yang, W. Yuan, Y. Wang, J. Yang, B. Yue, Multi-mode antibacterial strategies enabled by gene-transfection and immunomodulatory nanoparticles in 3D-printed scaffolds for synergistic exogenous and endogenous treatment of infections, Adv. Mater. 34 (18) (2022) 2200096, https://doi.org/10.1002/adma.202200096.

[41] Y. Jin, Y. Lu, X. Jiang, M. Wang, Y. Yuan, Y. Zeng, L. Guo, W. Li, Accelerated infected wound healing by probiotic-based living microneedles with long-acting antibacterial effect, Bioact. Mater. 38 (2024) 292–304, https://doi.org/10.1016/j.bioactmat.2024.05.008.

[42] T. Lu, F. Chen, Multiwfn: a multifunctional wavefunction analyzer, J. Comput. Chem. 33 (5) (2012) 580–592, https://doi.org/10.1002/jcc.22885.

[43] R.F.W. Bader, M.T. Carroll, J.R. Cheeseman, C. Chang, Properties of atoms in molecules: atomic volumes, J. Am. Chem. Soc. 109 (26) (1987) 7968–7979, https://doi.org/10.1021/ja00260a006.

[44] X. Shen, W. Liu, X. Gao, Z. Lu, X. Wu, X. Gao, Mechanisms of oxidase and superoxide dismutation-like activities of gold, silver, platinum, and palladium, and their alloys: a general way to the activation of molecular oxygen, J. Am. Chem. Soc. 137 (50) (2015) 15882–15891, https://doi.org/10.1021/jacs.5b10346.

[45] W. Dai, R. Shu, F. Yang, B. Li, H.M. Johnson, S. Yu, H. Yang, Y.K. Chan, W. Yang, D. Bai, Y. Deng, Engineered bio-heterojunction confers extra-and intracellular bacterial ferroptosis and hunger-triggered cell protection for diabetic wound repair, Adv. Mater. (2023) 2305277, https://doi.org/10.1002/adma.202305277.

[46] S. Cai, J. Liu, J. Ding, Z. Fu, H. Li, Y. Xiong, Z. Lian, R. Yang, C. Chen, Tumor-microenvironment-responsive biodegradable nanoagents based on lanthanide nucleotide self-assemblies toward precise cancer therapy, Angew. Chem. Int. Ed. 61 (48) (2022) e202204502, https://doi.org/10.1002/anie.202204502.

[47] S. Bhattacharyya, S.R. Ali, M. Venkateswarulu, P. Howlader, E. Zangrando, M. De, P.S. Mukherjee, Self-assembled Pd₁₂ coordination cage as photoregulated oxidase-like nanozyme, J. Am. Chem. Soc. 142 (44) (2020) 18981–18989, https://doi.org/10.1021/jacs.0c09567.

[48] D. Chen, Z. Xia, Z. Guo, W. Gou, J. Zhao, X. Zhou, X. Tan, W. Li, S. Zhao, Z. Tian, Y. Qu, Bioinspired porous three-coordinated single-atom Fe nanozyme with oxidase-like activity for tumor visual identification via glutathione, Nat. Commun. 14 (1) (2023) 7127, https://doi.org/10.1038/s41467-023-42889-w.

[49] L. Zhang, L. Zhang, H. Deng, H. Li, W. Tang, L. Guan, Y. Qiu, M.J. Donovan, Z. Chen, W. Tan, *In vivo* activation of pH-responsive oxidase-like graphitic nanozymes for selective killing of *Helicobacter pylori*, Nat. Commun. 12 (1) (2021) 2002, https://doi.org/10.1038/s41467-021-22286-x.

[50] R. Wang, M. Qiu, L. Zhang, M. Sui, L. Xiao, Q. Yu, C. Ye, S. Chen, X. Zhou, Augmenting immunotherapy via bioinspired MOF-based ROS homeostasis disruptor with nanozyme-cascade reaction, Adv. Mater. 35 (49) (2023) 2306748, https://doi.org/10.1002/adma.202306748.

[51] X. Lu, S. Gao, H. Lin, H. Tian, D. Xu, J. Shi, Bridging oxidase catalysis and oxygen reduction electrocatalysis by model single-atom catalysts, Natl. Sci. Rev. 9 (10) (2022) nwac022, https://doi.org/10.1093/nsr/nwac022.

[52] Y. Cheng, Y. Zhang, Z. Zhao, G. Li, J. Li, A. Li, Y. Xue, B. Zhu, Z. Wu, X. Zhang, Guanidinium-decorated nanostructure for precision sonodynamic-catalytic therapy of MRSA-infected osteomyelitis, Adv. Mater. 34 (50) (2022) 2206646, https://doi.org/10.1002/adma.202206646.

[53] C. Marx, S. Gardner, R.M. Harman, B. Wagner, G.R. Van de Walle, Mesenchymal stromal cell-secreted CCL2 promotes antibacterial defense mechanisms through increased antimicrobial peptide expression in keratinocytes, Stem Cells Transl. Med. 10 (12) (2021) 1666–1679, https://doi.org/10.1002/sctm.21-0058.

[54] I.v. Maldeghem, C.M. Nusman, D.H. Visser, Soluble CD14 subtype (sCD14-ST) as biomarker in neonatal early-onset sepsis and late-onset sepsis: a systematic review and meta-analysis, BMC Immunol. 20 (2019) 17, https://doi.org/10.1186/s12865-019-0298-8.

[55] S.D. Wright, R.A. Ramos, P.S. Tobias, R.J. Ulevitch, J.C. Mathison, CD14, a receptor for complexes of lipopolysaccharide (LPS) and LPS binding protein, Science 249 (4975) (1990) 1431–1433.

[56] Z. Li, W. Wei, M. Zhang, X. Guo, B. Zhang, D. Wang, X. Jiang, F. Liu, J. Tang, Cryptotanshinone-doped photothermal synergistic MXene@PDA nanosheets with antibacterial and anti-inflammatory properties for wound healing, Adv. Healthcare Mater. 12 (28) (2023) e2301060, https://doi.org/10.1002/adhm.202301060.

[57] Z. Yu, M. Li, L. Yang, H. Liu, G. Ding, S. Ma, L. Liu, S. Dong, Enhancing diabetic wound healing: a two-pronged approach with ROS scavenging and ROS-independent antibacterial properties, Nano Today 57 (2024) 102358, https://doi.org/10.1016/j.nantod.2024.102358.

[58] J.P. Horcajada, M. Montero, A. Oliver, L. Sorlí, S. Luque, S. Gómez-Zorrilla, N. Benito, S. Grau, Epidemiology and treatment of multidrug-resistant and extensively drug-resistant *Pseudomonas aeruginosa* infections, Clin. Microbiol. Rev. 32 (4) (2019) e00031, https://doi.org/10.1128/CMR.00031-19, 19.

[59] E.M. Darby, E. Trampari, P. Siasat, M.S. Gaya, I. Alav, M.A. Webber, J.M.A. Blair, Molecular mechanisms of antibiotic resistance revisited, Nat. Rev. Microbiol. 21 (5) (2022) 280–295, https://doi.org/10.1038/s41579-022-00820-y.

[60] W.P.J. Smith, B.R. Wucher, C.D. Nadell, K.R. Foster, Bacterial defences: mechanisms, evolution and antimicrobial resistance, Nat. Rev. Microbiol. 21 (8) (2023) 519–534, https://doi.org/10.1038/s41579-023-00877-3.

[61] J. Wang, S.P. Teong, S.N. Riduan, A. Armugam, H. Lu, S. Gao, Y.K. Yean, J.Y. Ying, Y. Zhang, Redox active Zn@MOFs as spontaneous reactive oxygen species releasing antimicrobials, J. Am. Chem. Soc. 146 (1) (2023) 599–608, https://doi.org/10.1021/jacs.3c10411.

[62] D. Cheng, R. Tian, R. Pan, Q. Yu, L. Wei, J. Liyin, Y. Dai, X. Wang, R. Tan, H. Qu, M. Lu, High-performance lung-targeted bio-responsive platform for severe colistin-resistant bacterial pneumonia therapy, Bioact. Mater. 35 (2024) 517–533, https://doi.org/10.1016/j.bioactmat.2024.02.017.